JOURNAL OF MECHANICAL ENGINEERING AND SCIENCES
ISSN: 2289-4659 e-ISSN: 2231-8380
VOLUME 20, ISSUE 1, 2026, 11036 - 11051
DOI: https://doi.org/10.15282/jmes.20.1.2026.2.0862

RESEARCH ARTICLE

Numerical-simulation hybrid analysis of orthogonal cutting of Inconel 718

Md Adan Maqsood[1], Mohd Reyaz Ur Rahim[1]*, Prem Kumar Bharti[1], Danish Iqbal[2], Ayesha Tariq[3]

[1]Department of Mechanical Engineering, Integral University, Lucknow 226026, Uttar Pradesh, India
[2]Department of Mechanical Engineering, Aligarh Muslim University, Aligarh 202002, Uttar Pradesh, India
[3]Department of Computer Science and Engineering, Integral University, Lucknow 226026, Uttar Pradesh, India

Abstract - Inconel 718 is widely employed in the aerospace and energy sectors due to its exceptional mechanical and thermal stability, yet it remains one of the most challenging materials to machine. This study develops and validates a comprehensive three-dimensional finite element model using ANSYS to simulate orthogonal cutting of Inconel 718. The developed model incorporates Johnson-Cook constitutive and damage laws to represent strain hardening, rate sensitivity, thermal softening, and failure behaviour under high-speed cutting conditions. A full factorial design combined with response surface methodology was employed to analyze how variations in cutting speed, rake angle, nose radius, clearance angle, and depth of cut affect key machining responses, including cutting force, von Mises stress, cutting temperature, and energy consumption. Simulation outputs were rigorously validated against available experimental data, achieving close agreement. Parametric and ANOVA analyses revealed that rake angle and cutting speed significantly affect chip segmentation and thermal gradients. Empirical regression models demonstrated high predictive accuracy and were used for multi-objective optimization, yielding an optimal parameter set that minimized cutting force, energy, and thermal load. The findings provide a validated, computationally efficient simulation framework with direct relevance to machining process optimization and tool performance prediction in superalloy applications.

Article History
Received : 8 October 2025
Revised : 25 February 2026
Accepted : 28 February 2026
Published : 31 March 2026

Keywords
Johnson-Cook model
Response surface method
Machining
Multi-objective optimization
Cutting forces
Chip formation

1. Introduction

Inconel 718, a nickel-chromium-based superalloy strengthened by precipitation hardening, is a critical material in aerospace, nuclear, marine, and power generation industries. Its ability to maintain structural stability, tensile strength, and corrosion resistance under extreme thermal and mechanical loading makes it a material of choice in components such as turbine blades, combustor parts, and exhaust manifolds [1,2]. However, these very attributes also contribute to its classification as a "difficult to machine" material. During machining, Inconel 718 displays high strain-rate sensitivity, severe work hardening, poor thermal conductivity, and a tendency to form serrated chips, especially at medium to high cutting speeds [3,4]. These factors cause elevated cutting forces, excessive heat generation, accelerated tool wear, and degradation of surface integrity. Segmented or serrated chip formation during orthogonal cutting is a prominent phenomenon in Inconel 718 and arises due to thermoplastic instability and adiabatic shear banding [5-7]. The low thermal diffusivity of the material leads to heat accumulation near the contact region between the tool and the chip, raising the local temperature, softening the material, and encouraging dynamic recrystallization and plastic flow localization [8]. This sequence ultimately induces chip segmentation. Umbrello and Arndt [9] have emphasized that conventional machining theories, including simplified shear-plane models, are inadequate to capture the complex thermal–mechanical coupling during chip formation in Inconel alloys.

Finite Element Modelling (FEM) has emerged as a powerful tool for studying the mechanics of superalloy machining. Orthogonal cutting tests modelled via FEM offer a controlled and efficient method for examining critical responses, such as cutting force evolution, equivalent stress, chip morphology, and temperature distributions [10]. While traditional experimental techniques provide valuable validation, they are often constrained by high costs, limited visualization of internal phenomena, and difficulties in reproducing extreme strain-rate conditions. In contrast, numerical simulation allows for precise parameter control, virtual experimentation, and repeatable investigation across a wide range of cutting conditions. FEM formulations in machining are generally categorized as Lagrangian, Eulerian, and Arbitrary Lagrangian Eulerian (ALE). The Lagrangian approach, where the mesh moves with the material, offers high spatial resolution but suffers from mesh distortion during large deformations. ALE, a hybrid method, has become increasingly popular for machining Inconel due to its ability to handle severe plastic deformation while maintaining numerical stability. Movahhedy et al. [11] and Pantale et al. [12] have demonstrated that ALE-based FEM offers superior accuracy in simulating shear-localized chip formation. A crucial component of any FEM simulation is the constitutive material model. The Johnson-Cook (JC) model remains the most widely used phenomenological model in machining simulations of Inconel 718. It accounts for strain hardening, strain-rate sensitivity, and thermal softening, making it suitable for high-speed cutting processes. Özel et al. [13] and Wang et al. [14] further refined this model by introducing strain-rate softening corrections derived from Split Hopkinson Pressure Bar (SHPB) tests, thereby enhancing its fidelity in simulating material flow under extreme conditions.

In addition to material modelling, the tool-chip interface behaviour significantly influences the simulation outcomes. Due to Inconel's strong adhesive tendencies, frictional heating becomes a dominant factor in predicting cutting temperatures and tool wear. Several studies have proposed enhanced friction models, including temperature- and velocity-dependent laws, to represent real-world interface conditions better. Yi et al. [15] showed that constant friction coefficients

*CORRESPONDING AUTHOR | M.R.U. Rahim | ✉ rrahim@iul.ac.in

are insufficient for simulating Inconel's cutting behaviour and proposed hybrid formulations for greater accuracy. Multiple researchers have built upon these foundations. Palmer et al. [16] demonstrated that plastic deformation occurs over a broad shear zone rather than a narrow plane, supporting the shift toward continuum-based modelling in FEM. Mithu et al. [17] employed AdvantEdge software with the JC model and Recht's fracture criterion, showing less than 13% error in force predictions and effectively replicating segmented chip morphology. However, they noted limitations due to neglected cooling effects and static friction assumptions. Tool geometry also plays a significant role. Veeranaath et al. [18] investigated the influence of tool edge radius and rake angle, finding that subtle modifications significantly impacted chip segmentation and cutting temperature. Mouli et al. [19] applied a 2D FEM to analyse stress and temperature distributions, highlighting the effect of feed and speed on segmentation trends. However, their simplified model lacked dynamic tool wear mechanisms and failed to account for frictional complexities. Advancements in 3D simulation techniques have yielded even more realistic insights. Paturi et al. [20] employed the DEFORM 3D software to simulate tool wear and heat transfer mechanisms during Inconel turning, validating their model against empirical benchmarks. They utilized Usui and Takeyama–Murata wear equations to track wear progression and frictional heating, though long-term wear evolution and surface integrity tracking were outside the study's scope.

Recent works have broadened the modelling focus. Liu et al. [21] evaluated residual stress profiles in machined Inconel 718 as a function of tool geometry, while Peng et al. [22] introduced flank wear effects directly into FEM simulations, improving force prediction accuracy. Pedroso et al. [23] published a comprehensive review outlining the limitations of current FEM techniques for machining Inconel and advocating adaptive meshing strategies, damage model integration, and real-time validation frameworks. Despite progress, several gaps persist in the literature. Many studies do not account for coating behaviour, oxidation, or tool deformation during extended cuts. Tool-chip workpiece thermal feedback mechanisms are often oversimplified, and temperature-dependent thermal and mechanical properties are rarely integrated across the full range of machining conditions. As noted by Jadam et al. [24] and Zhang et al. [25], the absence of multi-objective optimization frameworks further limits the applicability of FEM studies in production environments. To address these gaps, the present study proposes a comprehensive, validated 3D FEM framework for simulating the orthogonal cutting of Inconel 718 using ANSYS Explicit Dynamics. The model utilizes the Johnson-Cook constitutive and damage models, integrating cutting parameters such as clearance angle, speed, rake angle, and depth of cut to evaluate their effects on key responses, including cutting force, temperature distribution, von Mises stress, and chip morphology. Unlike prior efforts that often exclude validation, this study rigorously compares FEM outputs with available experimental data. ANOVA-based statistical analysis is employed to identify the most influential parameters, and regression-based empirical models are derived to aid real-time process optimization. By coupling advanced material modelling with accurate thermal–mechanical simulation and robust statistical interpretation, this research contributes a practical, scalable, and predictive framework for improving the machinability of Inconel 718 in high-performance applications.

2. Materials and Methods

The present study employs a three-dimensional finite element approach to simulate the orthogonal cutting of Inconel 718 using ANSYS Explicit Dynamics. The methodology encompasses detailed material characterization, geometric modelling of the workpiece and tool, selection of process parameters, structured experimental design, mesh generation and validation, boundary condition definition, and numerical simulation configuration. Careful consideration was given at each stage to ensure a realistic representation of cutting mechanics and computational accuracy.

2.1 Workpiece and Tool Modelling

The workpiece material modelled in this study is Inconel 718, a high-strength nickel-chromium superalloy known for its superior creep resistance and structural integrity under prolonged exposure to elevated temperatures. It is widely deployed in aerospace engines, turbine components, and nuclear reactor assemblies due to its ability to maintain mechanical performance at elevated temperatures. The alloy's machinability is affected by its intricate microstructure and multi-element composition, which contribute to its strain hardening and low thermal conductivity. To support material modelling and inform boundary condition assumptions, the nominal chemical composition of Inconel 718 is provided in Table 1. These values are consistent with the AMS 5662/3 standard and align with compositions used in prior machining simulations and experiments.

Table 1. Chemical composition of Inconel 718 (wt%)

Element	Ni	Cr	Fe	Nb + Ta	Mo	Ti	Al	Co	Others
wt%	50–55	17–21	Bal.	4.75–5.50	2.80–3.30	0.65–1.15	0.20–0.80	≤1.0	≤0.5

To accurately simulate the material's thermomechanical response during high-strain-rate deformation, the Johnson-Cook constitutive model was utilized. This phenomenological model is particularly suited to metal-cutting applications, as it integrates the effects of strain-rate sensitivity, strain hardening, and thermal softening into a unified formulation. The flow stress in the JC model is defined as a function of temperature, equivalent plastic strain, and strain rate. In addition, the Johnson-Cook damage model was implemented to capture material failure and enable chip separation via element erosion. This model defines damage initiation based on accumulated equivalent plastic strain, which depends on temperature, stress triaxiality, and strain rate. Once the damage criterion is met, elements are progressively removed to simulate material fracture and chip segmentation. The material constants used for both strength and damage modelling of

Inconel 718 are summarized in Table 2. These values were sourced from the literature and validated against SHPB experiments and high-speed machining studies to ensure consistency under orthogonal cutting conditions. These parameters ensure a realistic simulation of plastic deformation and fracture under cutting conditions involving extreme temperature and strain-rate gradients.

Table 2. Johnson Cook strength and damage model parameters for Inconel 718

Model	Parameter	Symbol	Value
Strength Model	Initial yield stress (MPa)	A	1240
	Hardening modulus (MPa)	B	1000
	Strain hardening exponent	n	0.45
	Strain rate coefficient	C	0.03
	Thermal softening exponent	m	1.0
	Room temperature (K)	T_{room}	298
	Melting temperature (K)	T_{melt}	1609
Damage Model	Failure strain parameter	D_1	0.13
	Stress triaxiality effect	D_2	0.19
	Strain rate effect	D_3	−0.15
	Temperature effect	D_4	0.014
	Failure strain scaling	D_5	1.5

The cutting tool was modelled as a rigid body, a commonly adopted approach in numerical machining studies to reduce computational cost while maintaining accurate contact mechanics. The tool material was defined as uncoated tungsten carbide, consistent with finishing tool geometries typically used for superalloy machining. Tool geometry was varied across a matrix of simulations, incorporating variations in clearance angle, rake angle, and nose radius, as shown in Table 3**.** These values were selected based on industry standard specifications and previous experimental investigations.

Table 3. Input parameters and their coded levels for FC-CCD

Input Variable	Unit	−α	−1	0	+1	+α
Cutting Speed	mm/sec	416.66	479.16	541.66	604.16	666.66
Rake Angle	degrees	0	4.375	8.75	13.125	17.5
Clearance Angle	degrees	0	2.5	5	7.5	10
Nose Radius	mm	0	0.075	0.15	0.225	0.3
Depth of Cut	mm	3	3.75	4.5	5.25	6

2.2 Selection of Input Parameters

A three-dimensional orthogonal cutting configuration was constructed, with the tool and workpiece modelled using solid brick elements. The workpiece was defined as a rectangular block with dimensions 80 mm in length, 20 mm in height, and 10 mm in width. These dimensions were chosen to ensure that the deformation zones during chip formation remained sufficiently isolated from boundary effects. The cutting process was represented as a planar interaction, with the tool moving horizontally into the stationary workpiece. To systematically investigate the influence of key process variables on cutting force, equivalent von Mises stress, temperature distribution, energy consumption, and chip morphology, five input parameters were selected based on their reported influence on chip formation, tool loading, and thermal behaviour in machining Inconel 718. The input parameters selected are depth of cut, rake angle, clearance angle, nose radius, and cutting speed. The selection was guided by experimental literature and practical industrial ranges for finishing operations of Inconel 718. A face-centred central composite design (FC-CCD) under the response surface methodology (RSM) framework was used to construct the experimental design. This statistical design enables efficient modelling of both linear and quadratic effects while minimizing the number of required simulations. Each input variable was assigned five coded levels, where −α and +α represent the axial points, −1 and +1 the factorial points, and 0 the centre value. These parameter levels ensure that the simulation matrix covers a broad design space, facilitating sensitivity analysis and robust model generation. Subsequent simulations using this matrix allow for regression modelling and response optimization.

2.3 Design of Experiments

After establishing input parameter ranges and coded levels, a full factorial design was used to generate the simulation matrix. This approach considers all possible combinations of selected parameter levels, enabling the model to capture interaction effects comprehensively. Five parameters, cutting speed, clearance angle, rake angle, nose radius, and depth of cut, were each considered at three distinct levels (−1, 0, +1); the total number of combinations in the full factorial framework was determined accordingly. Each simulation case represents a unique set of input conditions, and the corresponding machining responses (cutting force, chip morphology, temperature, and von Mises stress) were extracted for subsequent regression modelling and analysis of variance (ANOVA) [26-28]. The complete simulation plan based on the full factorial method is presented in Table 4. This comprehensive experimental design enables robust statistical

modelling and facilitates the identification of main effects and higher-order interactions among the selected input variables.

Table 4. Design of experiments matrix using the full factorial method

Run	Cutting speed mm/sec	Rake angle deg	Clearance deg	Nose radius mm	Depth of cut mm
1	0	0	α	0	0
2	1	1	1	-1	1
3	-1	1	1	-1	1
4	0	0	0	0	0
5	0	0	0	0	-α
6	1	1	-1	1	1
7	-1	1	-1	1	-1
8	-1	1	1	-1	-1
9	-1	1	1	1	-1
10	1	-1	-1	-1	1
11	-1	1	-1	-1	-1
12	0	0	0	0	α
13	0	0	0	0	0
14	-1	-1	1	-1	1
15	1	1	1	-1	-1
16	0	-α	0	0	0
17	0	0	0	0	0
18	1	-1	-1	-1	-1
19	1	1	-1	-1	1
20	-1	-1	-1	-1	1
21	-1	1	-1	1	1
22	-1	-1	1	-1	-1
23	-1	-1	1	1	1
24	0	0	0	-α	0
25	1	-1	1	-1	1
26	1	-1	1	1	-1
27	1	-1	-1	1	1
28	-1	1	1	1	1
29	1	1	1	1	-1
30	1	1	-1	1	-1
31	-1	-1	-1	1	-1
32	-α	0	0	0	0
33	1	-1	-1	1	-1
34	-1	1	-1	-1	1
35	-1	-1	-1	1	1
36	1	-1	1	1	1
37	-1	-1	1	1	-1
38	-1	-1	-1	-1	-1
39	0	α	0	0	0
40	0	0	0	0	0
41	0	0	0	0	0
42	0	0	-α	0	0
43	α	0	0	0	0
44	1	1	1	1	1
45	0	0	0	0	0
46	0	0	0	α	0
47	1	-1	1	-1	-1
48	0	0	0	0	0
49	1	1	-1	-1	-1
50	0	0	0	0	0

2.4 Boundary Conditions

To replicate practical orthogonal cutting conditions, appropriate mechanical and thermal boundary conditions were applied to both the tool and workpiece. The bottom surface of the workpiece was fully constrained in all translational degrees of freedom to prevent rigid body motion during deformation. The cutting tool was prescribed a constant velocity in the cutting direction corresponding to the specified cutting speed. The interaction between the tool and workpiece was defined using a surface-to-surface penalty-based contact formulation with friction modelled through a constant Coulomb friction coefficient. Although advanced friction laws incorporating pressure- and temperature-dependent behaviour have been reported to represent better tool–chip interaction in the machining of Inconel 718, a constant Coulomb friction model was adopted in the present study to ensure numerical stability and reduce computational complexity within the explicit dynamic framework. The primary objective of this work is to evaluate comparative trends in cutting force, stress distribution, temperature evolution, and chip morphology under varying cutting parameters. The constant friction assumption improves convergence robustness in large-deformation Lagrangian simulations involving severe mesh distortion and element erosion. While this simplification does not capture all tribological complexities, the predicted cutting forces and thermomechanical responses show good agreement with experimental data, confirming that the adopted approach is adequate for the study's objectives.

Thermomechanical coupling was enabled, allowing heat generation from both plastic deformation and frictional sliding at the tool–chip interface. Thermal conduction across the contact interface was considered to capture heat transfer between the tool and workpiece. However, heat losses due to convection and radiation were neglected owing to the short cutting duration characteristic of orthogonal machining simulations. The complete boundary and loading configuration, along with the structured three-dimensional finite element mesh, is illustrated in Figure 1, which shows the initial geometry, constraint conditions, and prescribed tool motion.

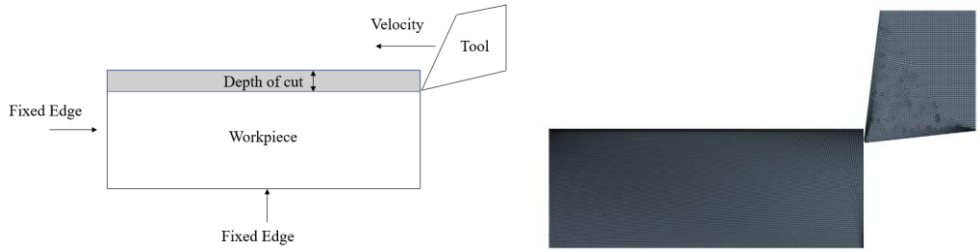

Figure 1. Schematic model of the orthogonal cutting with boundary conditions and its corresponding finite element mesh

2.5 Mesh Validation and Refinement

To ensure numerical accuracy while maintaining computational efficiency, a systematic mesh sensitivity study was conducted in the primary deformation region of the workpiece. A fully Lagrangian formulation with structured three-dimensional solid brick elements was employed. Local mesh refinement was applied along the tool–chip interface and primary shear zone, where high strain and temperature gradients were expected, while a comparatively coarser mesh was maintained in regions away from the cutting zone to reduce computational cost. The mesh was progressively refined using element sizes of 3 mm, 2 mm, 1.5 mm, and 1 mm within the primary deformation region. Element quality was controlled by maintaining the aspect ratio below 3 and ensuring acceptable skewness as defined by the solver. The total number of elements ranged from approximately 24,000 for the 3 mm mesh to about 86,000 for the refined 1 mm configuration. Mesh convergence was evaluated based on the maximum von Mises stress developed in the workpiece. The variation in maximum stress prediction decreased consistently with mesh refinement. The difference between the 1.5 mm and 1 mm meshes was only 0.26%, whereas the coarsest mesh (3 mm) exhibited a deviation of 2.71%, indicating insufficient spatial resolution in the shear zone. Based on these results, the 1 mm mesh was selected for all subsequent simulations, as further refinement yielded negligible changes in stress predictions while significantly increasing computational time. The results of the mesh sensitivity analysis are summarized in Table 5.

Table 5. Mesh sensitivity analysis based on maximum von Mises stress

Mesh Size (mm)	Maximum stress (MPa)	Difference (%)
3.0	1705.800	2.71
2.0	1753.292	1.26
1.5	1775.720	0.26
1.0	1780.400	–

2.6 Simulation

The cutting simulations were performed using the explicit time-integration scheme in ANSYS Explicit Dynamics. The explicit formulation was selected for its suitability to high-speed machining processes involving severe nonlinear plastic deformation, large strain gradients, and complex three-dimensional contact interactions. The total physical cutting time simulated was 0.5 ms, corresponding to the prescribed cutting velocity and tool travel distance. The analysis was executed in a single explicit dynamic step and the stable time increment was automatically computed by the solver according to

the Courant–Friedrichs–Lewy stability criterion, which relates the time step to the smallest characteristic element length and the elastic wave speed of the material. For the adopted 1 mm refined mesh, the stable time increment was on the order of 10^{-8} s, yielding approximately 20,000–30,000 explicit time increments per simulation. No manual time step scaling was imposed, and mass scaling was avoided to preserve the physical accuracy of the dynamic response. The workpiece material behaviour was defined using the Johnson–Cook constitutive model, which incorporates strain hardening, strain-rate sensitivity, and thermal softening. Chip initiation and segmentation were modelled using the Johnson–Cook damage criterion, where element erosion occurred once the accumulated damage parameter reached unity. Surface-to-surface contact between the rigid cutting tool and deformable workpiece was defined using a penalty-based contact formulation with Coulomb friction at the tool–chip interface. Appropriate displacement constraints were applied to prevent rigid-body motion of the workpiece. Numerical stability was verified by monitoring the energy balance throughout the simulation. The kinetic energy remained below 5% of the internal energy, confirming quasi-static cutting conditions despite the use of an explicit dynamic solver. Hourglass control was activated to prevent zero-energy deformation modes, and adaptive remeshing was deactivated to preserve chip continuity during segmentation.

2.7 Validation

To evaluate the predictive capability of the developed FEM framework, simulated cutting forces were compared with experimentally measured values under dry orthogonal cutting conditions. Figure 2 presents a side-by-side comparison of the simulation and experimental results across three representative test cases. In the first case, the experimentally recorded cutting force was 90.024 kN, while the simulation predicted 87.548 kN, yielding a deviation of 2.75%**.** In the second case**,** the experimental force reached 105 kN, with the simulation estimating 100.310 kN, corresponding to a 4.47% deviation, which is the highest among the three cases, yet still within an acceptable error margin for machining simulations. In the third case, the model predicted 123.610 kN, compared with the experimental value of 127.523 kN, resulting in a 3.07% deviation. Across all cases, the simulation consistently underpredicted the cutting force yet followed the same trend and magnitude progression observed in the experiments. These results highlight the model's robustness and its ability to accurately replicate the underlying physics of the cutting process, particularly the evolution of force within the primary deformation zone. The minor discrepancies between simulated and experimental values can be attributed to several modelling assumptions. These include idealized boundary conditions, rigid tool approximation, and the absence of real-world factors such as tool wear, minor vibrations, and microscale frictional irregularities. Nonetheless, the simulation incorporates strain-rate sensitivity, strain hardening, and thermal softening via the Johnson-Cook material and damage models, enabling an accurate representation of the thermomechanical coupling and plastic flow behaviour inherent in machining Inconel 718. The small percentage deviations, ranging from 2.75% to 4.47%, confirm that the FEM model is both quantitatively and qualitatively consistent with experimental observations. This strong correlation validates the proposed simulation approach as a reliable, computationally efficient tool for predicting cutting forces and optimizing machining parameters in high-performance alloy systems.

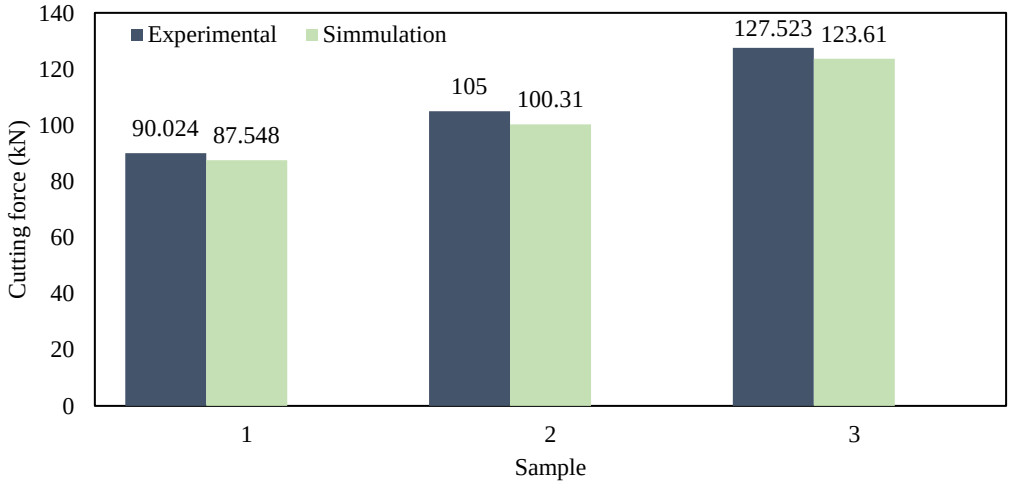

Figure 2. Comparison of experimental and FEM cutting forces under orthogonal cutting conditions

2.8 Postprocessing

Postprocessing of simulation outputs was performed using ANSYS's built-in capabilities, and the results were further analyzed using DesignExpert. The cutting force was extracted using probe reactions at the tool base. Temperature contours and von Mises stress fields were visualized to study thermal and mechanical load distributions in the primary and secondary deformation zones. Chip formation was analysed through sequential deformation frames to assess segmentation frequency and curling behaviour.

3. Results and Discussion

The simulations evaluated the influence of key machining variables such as cutting speed, clearance angle, rake angle, nose radius, and depth of cut on several machining responses such as cutting force, von Mises stress, temperature

distribution, and energy consumption. The design was structured as a full-factorial Design of Experiments, enabling robust statistical analysis and thorough exploration of parameter interactions.

3.1 Cutting Force Analysis

Cutting force is a primary indicator of machinability and tool load during metal cutting. The cutting force was extracted from a reaction force probe placed on the tool face. The results indicate that cutting speed, rake angle, and nose radius significantly affect the cutting force. High cutting speeds combined with a small nose radius and high rake angle minimized cutting forces, whereas low rake angles or greater depths of cut tended to elevate them. As shown in Table 6, cutting forces ranged from 56.43 kN to 123.61 kN.

Table 6. Effect of Input parameters on maximum cutting force, von Mises stress, temperature, and energy consumption

Run	Cutting speed (mm/sec)	Rake angle (deg)	Clearance angle (deg)	Nose radius (mm)	Depth of cut (mm)	Cutting force (kN)	von Mises stress (MPa)	Temperature (°C)	Maximum energy (J)
1	541.666	8.750	10.0	0.150	4.50	87.548	1780.400	297.040	4866.000
2	604.166	13.125	7.5	0.075	5.25	92.579	1615.600	378.670	5074.600
3	479.167	13.125	7.5	0.075	5.25	92.400	1629.100	341.260	5292.300
4	541.666	8.750	5.0	0.150	4.50	87.649	1625.500	298.470	4862.400
5	541.666	8.750	5.0	0.150	3.00	56.434	1616.400	285.070	3320.100
6	604.166	13.125	2.5	0.225	5.25	100.310	1629.400	353.820	5264.700
7	479.167	13.125	2.5	0.225	3.75	82.332	1622.700	385.300	4642.200
8	479.167	13.125	7.5	0.075	3.75	65.955	1647.200	329.340	3582.900
9	479.167	13.125	7.5	0.225	3.75	83.431	1613.900	410.600	4664.300
10	604.166	4.375	2.5	0.075	5.25	123.610	1666.200	486.380	5791.900
11	479.167	13.125	2.5	0.075	3.75	73.020	1611.800	327.740	4565.500
12	541.666	8.750	5.0	0.150	6.00	116.270	1864.700	368.960	5940.400
13	541.666	8.750	5.0	0.150	4.50	87.649	1625.500	298.470	4862.400
14	479.167	4.375	7.5	0.075	5.25	126.530	1624.600	464.090	5626.400
15	604.166	13.125	7.5	0.075	3.75	70.604	1615.600	354.190	3697.800
16	541.666	0.000	5.0	0.150	4.50	146.950	1906.100	409.350	5369.200
17	541.666	8.750	5.0	0.150	4.50	87.649	1625.500	298.470	4862.400
18	604.166	4.375	2.5	0.075	3.75	112.360	1642.400	555.310	4983.100
19	604.166	13.125	2.5	0.075	5.25	90.090	1631.000	357.810	5497.400
20	479.167	4.375	2.5	0.075	5.25	132.620	1629.900	448.080	5642.600
21	479.167	13.125	2.5	0.225	5.25	90.218	1624.000	348.700	5163.300
22	479.167	4.375	7.5	0.075	3.75	82.710	1966.600	372.660	4664.600
23	479.167	4.375	7.5	0.225	5.25	115.610	1631.400	391.640	5572.300
24	541.666	8.750	5.0	0.000	4.50	101.530	1620.100	377.710	5199.100
25	604.166	4.375	7.5	0.075	5.25	127.470	1621.300	490.000	5784.200
26	604.166	4.375	7.5	0.225	3.75	104.140	1616.400	417.970	4936.100
27	604.166	4.375	2.5	0.225	5.25	115.410	1647.5	415.620	5651.800
28	479.167	13.125	7.5	0.225	5.25	99.430	1624.700	356.430	5073.100
29	604.166	13.125	7.5	0.225	3.75	83.400	1614.200	430.160	4809.400
30	604.166	13.125	2.5	0.225	3.75	83.139	1609.100	358.120	4798.500
31	479.167	4.375	2.5	0.225	3.75	106.140	1800.300	375.580	4694.700
32	416.666	8.750	5.0	0.150	4.50	87.191	1605.800	374.220	4800.300
33	604.166	4.375	2.5	0.225	3.75	97.034	1624.700	397.030	4851.500
34	479.167	13.125	2.5	0.075	5.25	91.615	1645.900	346.130	5322.000
35	479.167	4.375	2.5	0.225	5.25	117.450	1626.900	396.770	5593.800
36	604.166	4.375	7.5	0.225	5.25	118.040	1646.300	400.690	5598.800
37	479.167	4.375	7.5	0.225	3.75	96.807	1709.000	422.020	4834.100
38	479.167	4.375	2.5	0.075	3.75	88.588	1811.400	389.270	4816.900
39	541.666	17.500	5.0	0.150	4.50	75.291	1642.000	361.790	4611.500
40	541.666	8.750	5.0	0.150	4.50	87.649	1625.500	298.470	4862.400

Table 6. Continued

Run	Cutting speed (mm/sec)	Rake angle (deg)	Clearance angle (deg)	Nose radius (mm)	Depth of cut (mm)	Cutting force (kN)	von Mises stress (MPa)	Temperature (°C)	Maximum energy (J)
41	541.666	8.750	5.0	0.150	4.50	87.649	1625.500	298.470	4862.400
42	541.666	8.750	0.0	0.150	4.50	90.600	1802.700	361.790	4611.500
43	666.666	8.750	5.0	0.150	4.50	95.943	1627.200	385.270	5123.500
44	604.166	13.125	7.5	0.225	5.25	98.252	1627.500	444.960	5239.800
45	541.666	8.750	5.0	0.150	4.50	87.649	1625.500	298.470	4862.400
46	541.666	8.750	5.0	0.300	4.50	86.850	1630.600	352.760	4717.700
47	604.166	4.375	7.5	0.075	3.75	107.060	1625.200	399.120	4783.300
48	541.666	8.750	5.0	0.150	4.50	87.649	1625.500	298.470	4862.400
49	604.166	13.125	2.5	0.075	3.75	75.195	1638.200	350.600	4340.000
50	541.666	8.750	5.0	0.150	4.50	87.649	1625.500	298.470	4862.400

The empirical relationship between input parameters and cutting force, expressed in Eq. (1), was developed using RSM

$$Cutting\ force = 95.81 + 0.7028A - 10.95B - 0.6955C + 0.8481D + 0.5973E - 0.7503AB + 0.1817AC - 0.8996AD + 1.64AE + 0.4638BC + 1.95BD - 0.0035BE - 0.1727CD - 1.30CE + 1.79\,DE \quad (1)$$

where A: cutting speed, B: rake angle, C: clearance angle, D: nose radius, E: depth of cut.

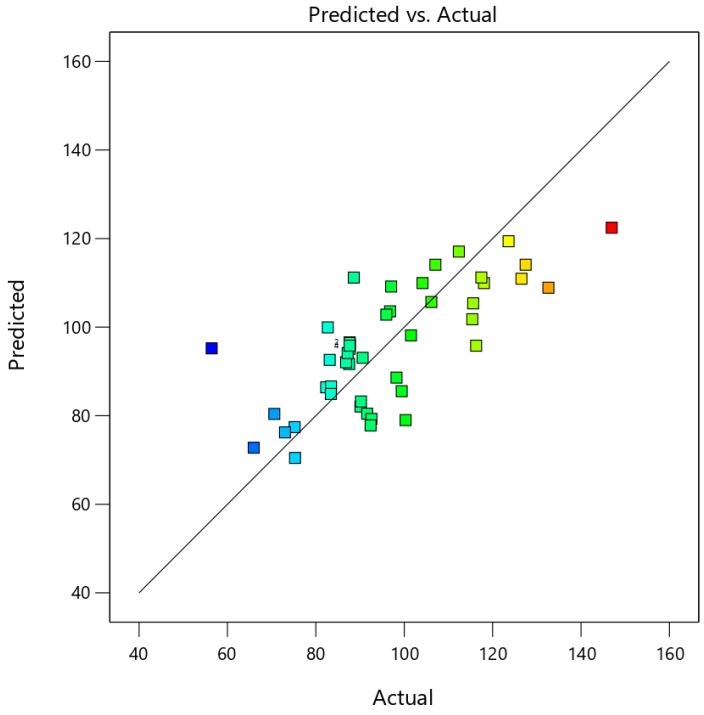

Figure 3. Predicted versus actual results of cutting force in kN

The model's predictive capability is illustrated in Figure 3, showing a strong correlation between actual and predicted cutting force values. Additionally, 3D surface plots, shown in Figure 4, depict the interactions among various parameters on cutting force. The observed increase in cutting force with increasing depth of cut and cutting speed is consistent with previously reported findings for orthogonal machining of Inconel 718 and other nickel-based superalloys [29–31]. Due to the high strength, strain-hardening behaviour, and low thermal conductivity of Inconel 718, greater material removal volumes result in higher shear deformation resistance and elevated tool–chip interface stresses [29,32]. Similar trends have been reported in experimental and numerical studies, where cutting force was found to increase proportionally with the undeformed chip thickness and decrease with increasing rake angle, due to improved shear-plane mechanics [30,33]. The reduction in cutting force at higher rake angles observed in this study is also consistent with classical metal-cutting theory [34], which predicts that positive rake angles reduce the shear plane area and frictional resistance at the tool–chip interface. These consistencies confirm the reliability of the implemented constitutive and damage models.

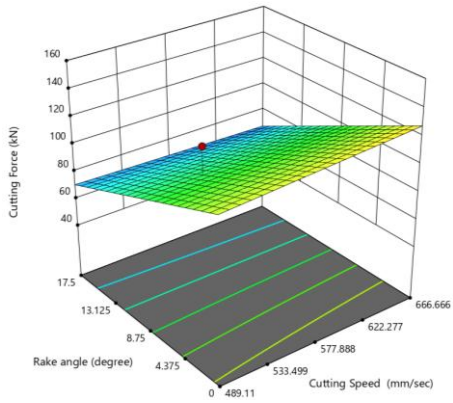

(a) Cutting speed and rake angle on cutting force

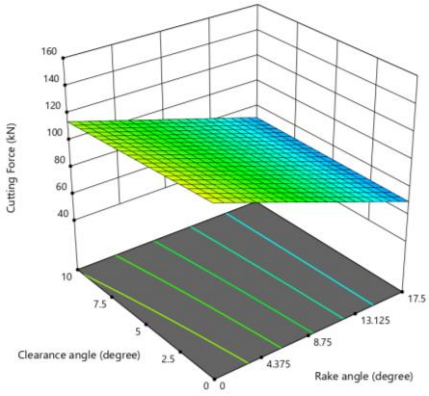

(b) Rake angle and clearance angle on cutting force

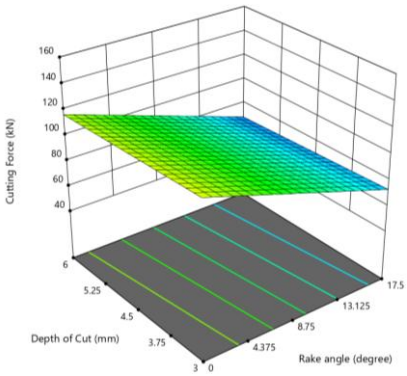

(c) Rake angle and depth of cut on cutting force

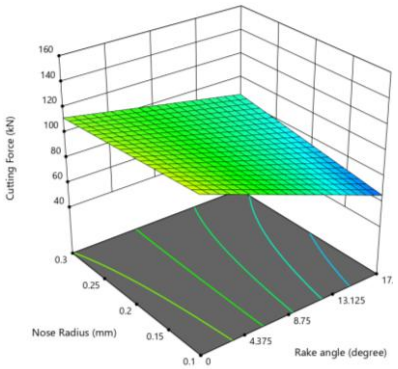

(d) Rake angle and nose radius on cutting force

Figure 4. Effect of cutting speed, rake angle, clearance angle, depth of cut, and nose radius on cutting force

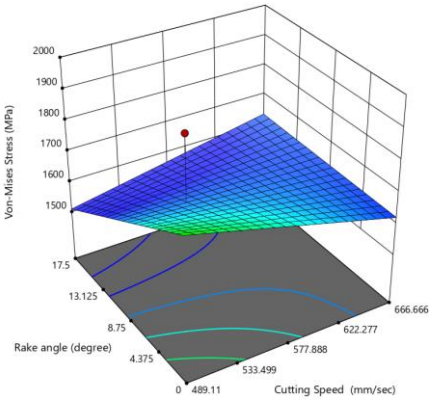

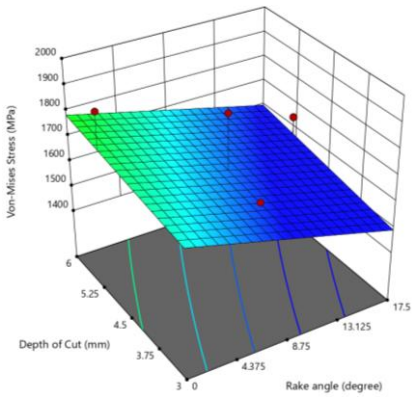

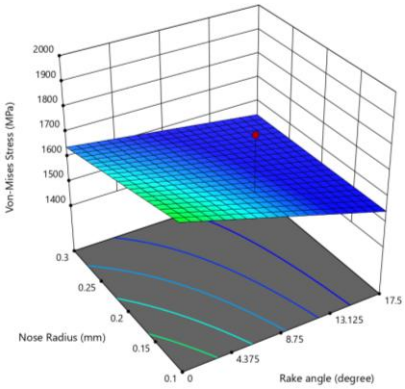

(a) Rake angle and cutting speed on von-Mises stress (b) Rake angle and depth of cut (c) Rake angle and nose radius

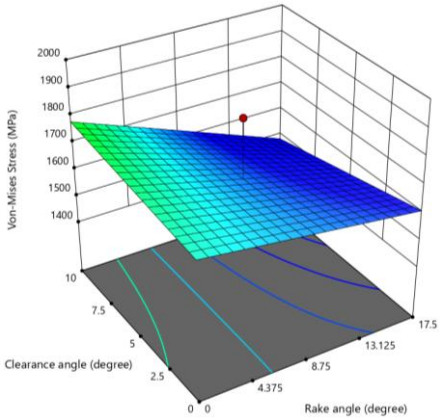

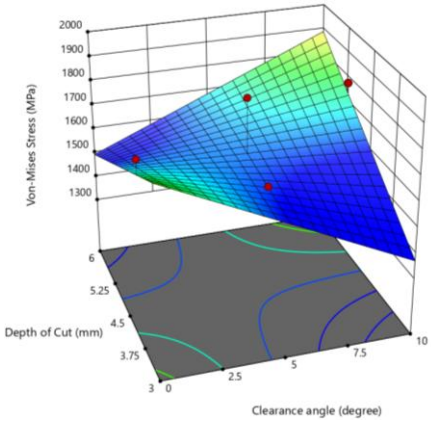

(d) Rake angle and clearance angle (e) Depth of cut and clearance angle

Figure 5. Effect of cutting speed, rake angle, clearance angle, depth of cut, and nose radius on von Mises stress

3.2 von Mises Stress

The von Mises stress was measured to evaluate material deformation under compressive and shear loads. Peak stresses were typically observed in the primary shear zone and at the tool-chip contact region. Stresses exceeded 1900 MPa in some high-speed and high-depth-of-cut runs, confirming the onset of intense plastic deformation and possible chip segmentation. Variation in stress is clearly depicted in Table 6. The empirical relationship between the input parameters and the equivalent stress is given by Eq. (2).

$$\text{von Mises Stress} = 1646.33 - 7.50A - 42.23B - 6.59C - 22.04D + 19.54E + 18.77AB - 1.17AC + 2.83AD - 4.77AE - 8.56BC + 8.96BD + 1.35BE - 5.62CD + 37.50CE - 16.38DE \quad (2)$$

The interaction effects of input parameters are further visualized in 3D response surface plots shown in Figure 5, which indicate that von Mises stress increases with greater depth of cut, while moderate rake angles help distribute stress more evenly, reducing tool wear potential.

3.3 Temperature Distribution

Thermal behaviour is a critical concern when machining Inconel 718, due to its low thermal conductivity and high strength retention at elevated temperatures. The temperature at the tool-chip interface ranged from 285 °C to 486 °C, as shown in Table 6, with higher values corresponding to higher cutting speeds and depths of cut. A steep rake angle contributed to more efficient chip evacuation and reduced localized heat. An empirical model was developed to predict interface temperatures, which is expressed in Eq. (3).

$$\text{Temperature} = 308.48 + 7.92A - 18.63B + 0.7067C + 0.6582D - 1.89E - 5.13AB - 2.30AC - 6.64AD + 4.09AE + 8.53BC + 16.37BD - 2.31BE + 8.69CD - 7.17CE + 2.35DE + 17.20A^2 + 20.09B^2 + 12.97C^2 + 15.88D^2 - 6.53E^2 \quad (3)$$

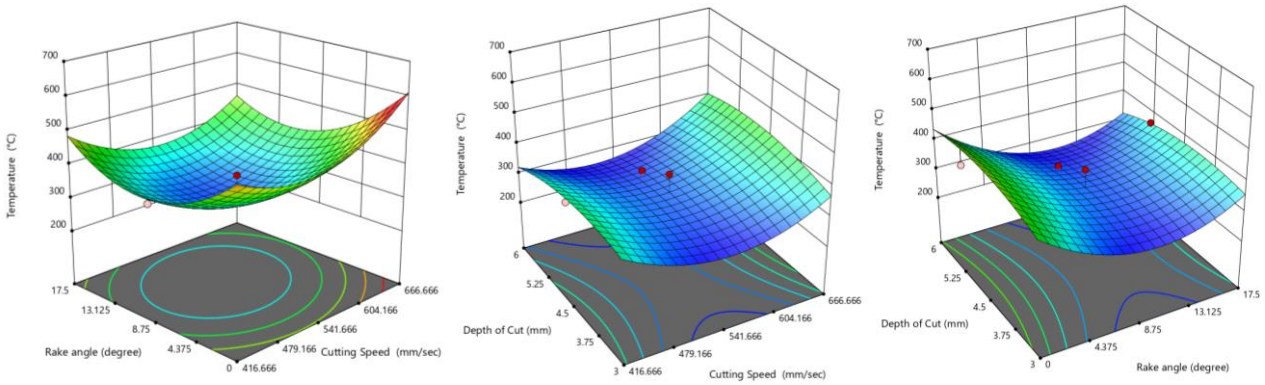

(a) Rake angle and cutting speed (b) Cutting speed and depth of cut (c) rake angle and depth of cut

(d) Rake angle and clearance angle (e) Rake angle and nose radius

Figure 6. Effect of cutting speed, rake angle, depth of cut, clearance angle, and nose radius on temperature

The response surfaces, as shown in Figure 6, reveal that shallow rake angles amplify heat concentration near the tool tip, whereas positive rake angles facilitate smoother chip flow and reduced thermal load. The predicted temperature distribution, particularly the peak temperature concentration at the tool–chip interface, agrees well with established machining behaviour of nickel-based superalloys [35–37]. Inconel 718 exhibits low thermal conductivity, which limits heat dissipation into the workpiece and promotes heat localization within the primary and secondary deformation zones [35,38]. Previous investigations have reported that increasing cutting speed significantly elevates the interface temperature due to greater plastic work converted to heat and reduced thermal diffusion time [36,39]. The present simulation results demonstrate similar thermal behaviour, confirming that the Johnson adequately captures thermal softening and strain-rate effects–Cook constitutive formulation adopted in this study [40].

3.4 Energy Consumption

The simulation also provided insights into the total energy input, including contributions from internal, kinetic, and plastic deformation. The results revealed energy values ranging from approximately 3300 J to nearly 6000 J, as depicted in Table 6, depending on the input configuration. Energy consumption increased significantly with the depth of cut and moderately with cutting speed. The empirical relationship between the input parameters and energy is given by Eq. (4).

$$\text{Energy} = 4965.51 + 3.21A - 158.40B - 38.86C + 46.70D + 23.93E - 22.87AB - 16.34AC + 10.62AD + 89.09AE - 40.78BC + 47.46BD + 14.79BE + 26.87CD - 60.98CE + 46.93DE \quad (4)$$

The interaction effects are illustrated in Figure 7, where deeper cuts and smaller nose radii result in steeper energy curves due to increased plastic deformation volume.

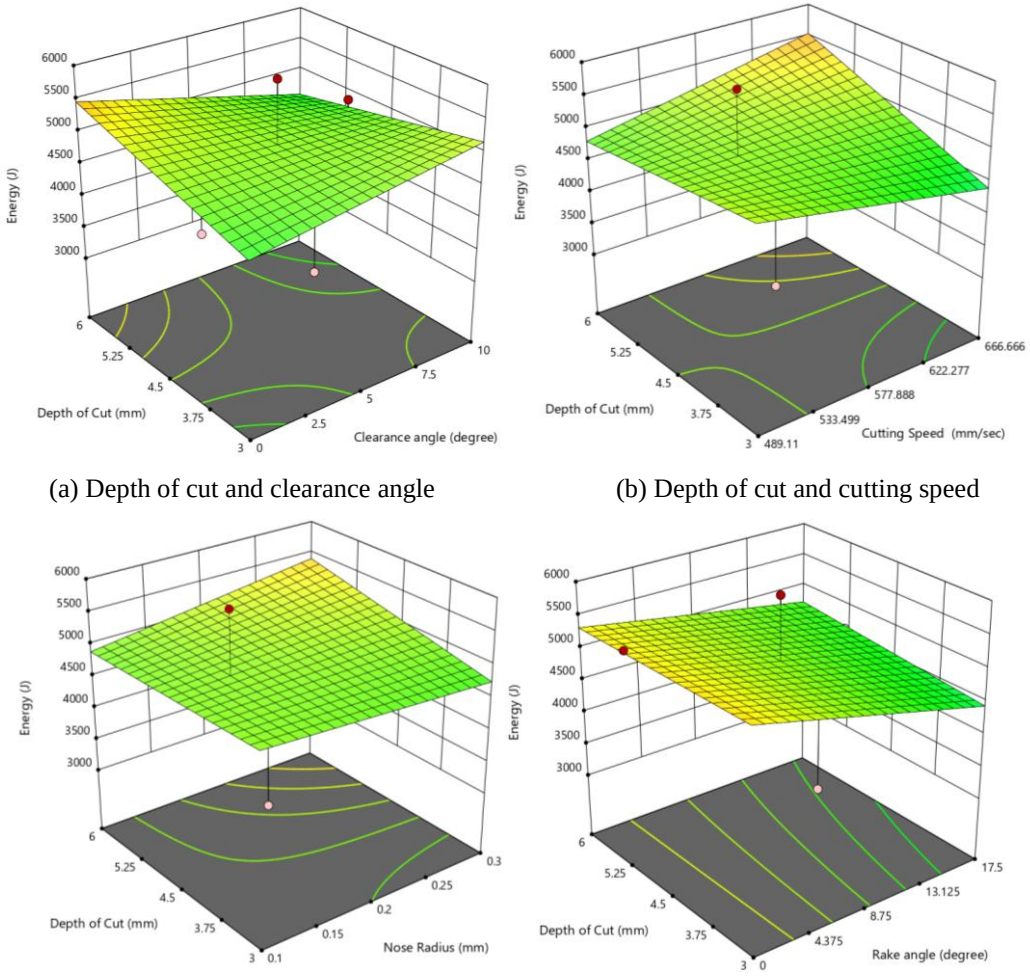

(a) Depth of cut and clearance angle

(b) Depth of cut and cutting speed

(c) Depth of cut and nose radius

(d) Depth of cut and rake angle

Figure 7. Effect of depth of cut, clearance angle, cutting speed, nose radius, and rake angle on energy consumption

3.5 Chip Morphology

Although chip geometry was not directly extracted as a separate three-dimensional solid model, chip morphology was evaluated through sequential deformation contours obtained from the explicit dynamic simulation. The chip formation process was analysed by examining stress, strain, temperature, and damage evolution at different solution increments (time steps) during tool advancement. In ANSYS Explicit Dynamics, the "step number" corresponds to a specific incremental time point in the transient cutting simulation, enabling the progressive development of chip formation to be tracked. It should be noted that quantitative geometric metrics such as chip thickness ratio, segmentation frequency, and shear band spacing were not directly extracted in the present study. Due to the large-deformation fully Lagrangian formulation and the implementation of element erosion for chip separation, significant mesh distortion and progressive element removal limit the reliability of precise geometric measurements throughout the cutting process. Consequently, chip morphology was characterized qualitatively by monitoring the evolution of stress, strain, temperature, and damage contours at different solution increments. The primary objective of this analysis is to identify the transition between continuous and segmented chip formation and to interpret the governing thermomechanical mechanisms rather than to perform detailed geometric quantification.

Conditions characterized by high cutting force, elevated von Mises stress, and increased interface temperature strongly favored segmented or serrated chip formation. This behaviour is associated with adiabatic shear localization, a well-established characteristic of machining Inconel 718 due to its strain-rate sensitivity and thermal softening. Under such conditions, intense plastic deformation localizes within narrow shear bands, leading to periodic chip segmentation. This

phenomenon is illustrated in Figures 8(a-b), where higher mechanical and thermal loading correlates with unstable chip flow and fully developed serrated chip profiles. In contrast, machining conditions involving moderate cutting speeds, optimized rake angles, and lower thermal gradients produced relatively stable material flow. Figures 8(c-d) correspond to different solution increments extracted from the same simulation case and demonstrate the temporal evolution of chip formation. Figure 8(c) shows an earlier time step in which chip formation is predominantly continuous, with uniform plastic flow along the primary shear zone. Figure 8(d) corresponds to a later incremental step under identical cutting conditions, where localized strain concentration begins to intensify, indicating the onset of delayed segmentation. However, complete serrated chip separation has not yet occurred at this stage.

The inclusion of step numbers in the figures therefore indicates the specific incremental time from which the results were extracted, highlighting the progressive transition from stable continuous chip flow to localized shear band development. These observations confirm that the implemented Johnson–Cook constitutive and damage models effectively capture the dynamic evolution of chip morphology during orthogonal cutting of Inconel 718. Although chip formation was not directly measured in 3D geometry, the morphology was inferred from mechanical and thermal responses. Conditions exhibiting high cutting force, stress, and temperature correlated strongly with segmented or saw-tooth chip formation, an outcome of adiabatic shear localization, which is characteristic of machining Inconel 718. This trend is evident in Figures 8(a) and 8 (b), where higher input energy correlates with segmented chip profiles. Conversely, scenarios involving moderate speeds and rake angles (e.g., Run 5) produced smoother force transitions and more continuous chip flow, as seen in Figures 8(c-d). These chip formation patterns validate the JC-based material model and the failure criteria used in the simulations.

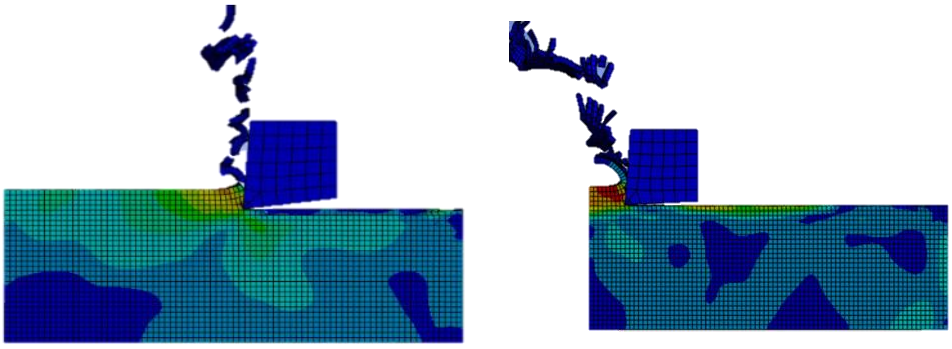

(a) Serrated chip formation (b) Unstable chip flow

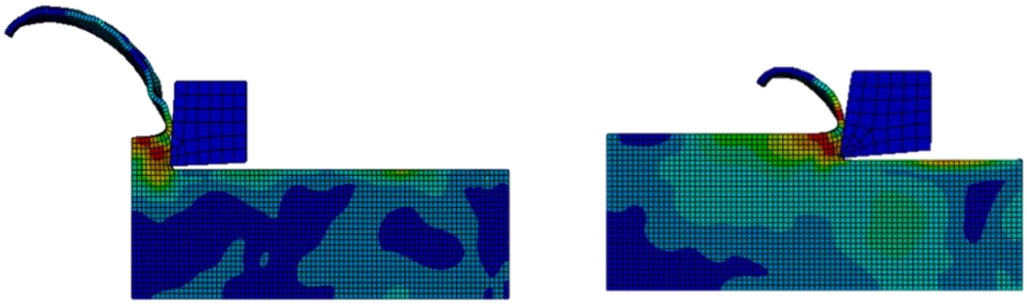

(c) Continuous chip formation (d) Delayed chip segmentation: continuous chip

Figure 8. Chip Formation Characteristics: (a) Serrated chip formation; (b) Unstable chip flow

3.6 Multi-objective Optimization Approach

The final phase of analysis involved optimization using Response Surface Methodology in conjunction with a desirability function approach. The objective was to simultaneously reduce cutting force, temperature, and energy while ensuring stress levels and chip quality remained within acceptable bounds. The optimal conditions were achieved at a cutting speed of 604.166 mm/s, a rake angle of 13.125°, a clearance angle of 7.5°, a nose radius of 0.225 mm, and a depth of cut of 5.25 mm. This combination yielded a cutting force of 92.579 kN, a temperature of 378.67 °C, a von Mises stress of 1966.6 MPa, and an energy consumption of 5940.4 J. Figure 9 illustrates the numerical optimization solution obtained using the desirability function approach within the Response Surface Methodology framework. Figure 9 presents the optimal combination of cutting parameters that simultaneously minimizes cutting force, temperature, and energy consumption while maintaining acceptable stress levels. The ramp plots display the selected factor levels along with their corresponding predicted response values. Each response is transformed into a dimensionless desirability scale ranging from 0 to 1, where higher values indicate better fulfilment of the optimization objective. The overall composite desirability value represents the combined effect of all responses and confirms the robustness of the optimized solution. The improved clarity of the revised figure enables a more straightforward interpretation of the relationship between process parameters and optimized machining performance. The desirability plot, shown in Figure 10, illustrates the trade-offs among responses and confirms that the global desirability value exceeds 0.85, indicating strong overall performance.

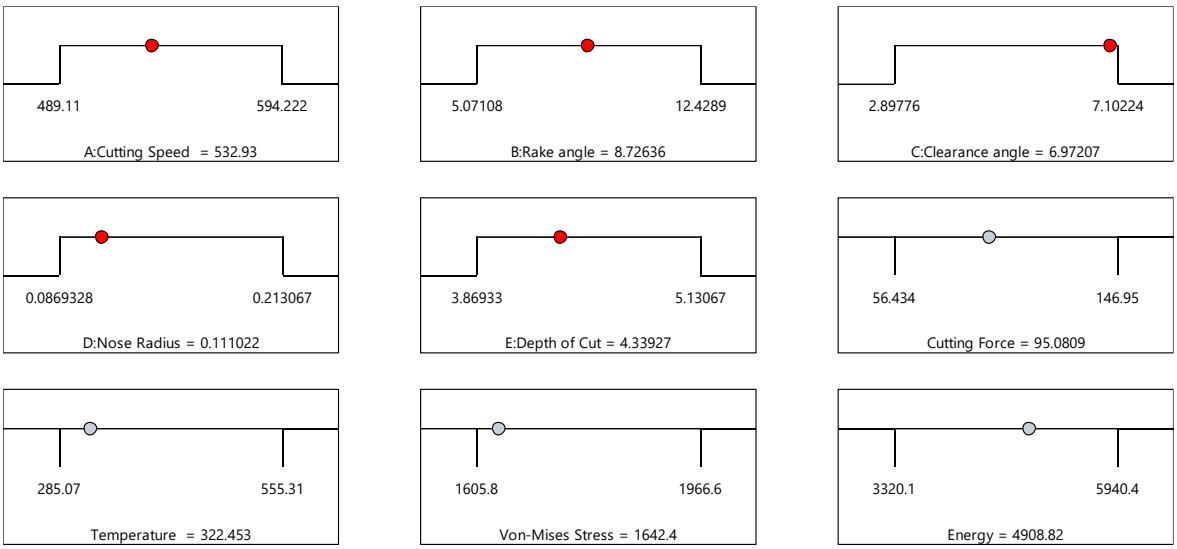

Figure 9. Optimization solution

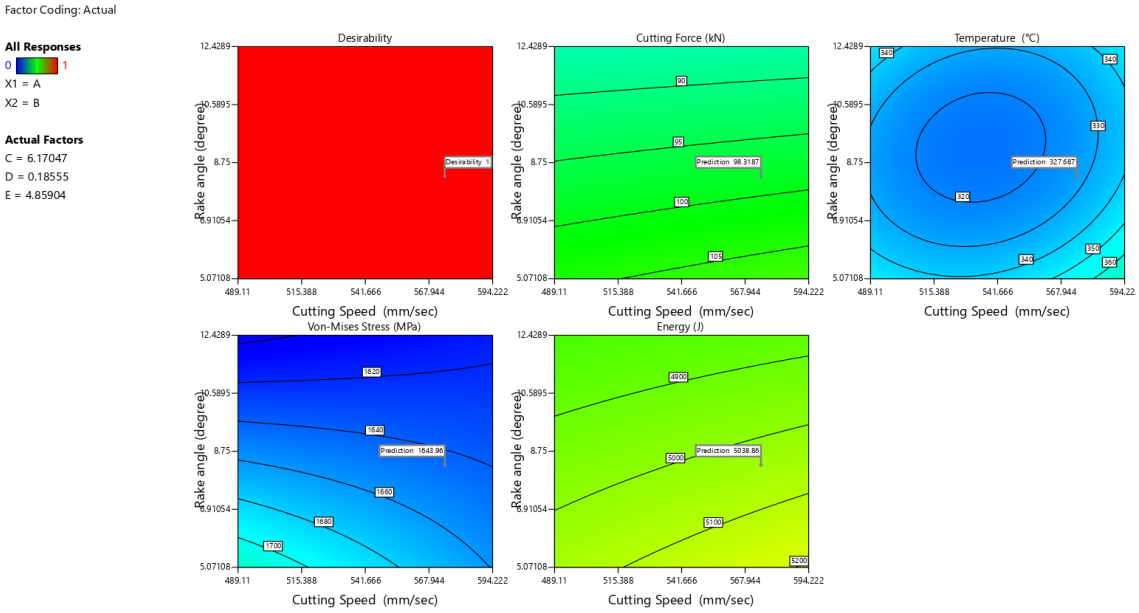

Figure 10. Desirability plot

4. Conclusions

This study presents a robust and validated three-dimensional finite element model for simulating the orthogonal cutting of Inconel 718, incorporating the Johnson-Cook constitutive and damage models. The simulation framework accurately captures the complex thermo-mechanical interactions typical of Inconel 718 machining, including high-strain-rate deformation, strain hardening, thermal softening, and chip segmentation. The effects of five critical process parameters, cutting speed, clearance angle, rake angle, nose radius, and depth of cut were systematically investigated through a full factorial design and Response Surface Methodology. The following insights and conclusions are drawn based on the analysis of output variables:

i) The cutting force varied significantly with process parameters, ranging from 56.43 kN to 146.95 kN. Physically, this response is governed by the shear resistance in the primary deformation zone. A higher rake angle reduced shear plane length and cutting resistance, while an increased cutting speed decreased contact time and friction, both leading to reduced force. Conversely, larger depths of cut elevated the material removal rate and chip load, increasing cutting force. The strong interaction between tool geometry and velocity underscores the need for a balanced configuration in high-speed cutting environments.

ii) Equivalent stress levels peaked above 1900 MPa, particularly under low rake angle and high depth of cut conditions. These high-stress regions were localized at the tool-chip interface, where material undergoes intense compressive and shear deformation. The observed trend aligns with plasticity theory, where deeper cuts expand the plastic zone and smaller rake angles concentrate compressive loads. Stress distribution analysis revealed that optimized geometries promote more uniform stress fields, reducing localized tool wear and structural degradation in the machined surface.

iii) The maximum interface temperature reached 555 °C under extreme process conditions. Due to Inconel 718's low thermal conductivity, heat generated through plastic deformation and friction accumulates in the cutting zone, causing thermoplastic instability. Positive rake angles and lower depths of cut facilitated better chip evacuation and reduced heat entrapment, while high cutting speeds enhanced adiabatic heating. The simulation confirmed the predominance of frictional heating at the tool-chip interface, supporting the need for thermal management strategies in superalloy machining.

iv) Total energy input ranged from 3300 J to 5940 J, reflecting the cumulative mechanical work and thermal energy involved in deformation and chip separation. Increased cutting speed and depth of cut elevated energy demands due to greater plastic deformation volume and increased contact forces. Smaller nose radii also led to higher energy concentrations by reducing contact area and increasing stress intensity. The results demonstrate that energy efficiency can be improved through appropriate tool geometry and moderate process parameters.

v) Although not directly extracted from 3D geometry, chip morphology was inferred from deformation history and thermal/mechanical response data. High stress, temperature, and energy conditions consistently aligned with segmented (serrated) chip formation—characteristic of adiabatic shear banding in thermally softening materials like Inconel 718. Conversely, smoother chip flow was associated with moderate cutting speeds and optimized rake angles, indicating a transition from unstable to stable chip formation mechanisms. This validates the physics embedded in the Johnson–Cook damage model and confirms its suitability for capturing dynamic chip behaviour.

vi) The final optimization, guided by desirability-based RSM, identified an optimal parameter combination: cutting speed of 604.16 mm/s, rake angle of 13.125°, clearance angle of 7.5°, nose radius of 0.225 mm, and depth of cut of 5.25 mm. This configuration minimized cutting force (92.58 kN), temperature (378.67 °C), and energy (5074.6 J), while maintaining von Mises stress within safe limits (1615.6 MPa). The high global desirability index (> 0.85) confirms the model's reliability in balancing multiple machining objectives.

Acknowledgements
The authors would like to express their sincere gratitude to Integral University, India, for providing institutional support, research facilities, and encouragement to carry out this study.

Funding
This study was not supported by any grants from funding bodies in the public, private, or not-for-profit sectors.

Declaration of Competing Interest
The author declares no conflicts of interest.

CRediT Authorship Contribution Statement
Md Adan Maqsood (Methodology; Data curation; Writing – original draft; Resources)
Mohd Reyaz Ur Rahim (Investigation; Writing -original draft; Methodology; Conceptualization; Supervision)
Prem Kumar Bharti (Formal analysis)
Danish Iqbal (Formal analysis)
Ayesha Tariq (Writing -review & editing)

Availability of Data and Materials
The data supporting this study's findings are available on request from the corresponding author.

Ethics Declarations
This study did not involve human participants or animals. Ethical approval was therefore not required.

Generative Artificial Intelligence Declarations
The authors stated that generative AI was not used to generate content, ideas, or theories. We have just utilised AI to enhance readability and refine the language. This was used with extreme human control and oversight. The authors take full responsibility for reviewing and approving the content.

References
[1] A. Barcelo Singh, "Oxidation resistance of additively manufactured Inconel 718 for gas turbine applications," Doctoral dissertation, Carleton University, 2020.
[2] G. Gudivada and A. K. Pandey, "Recent developments in nickel-based superalloys for gas turbine applications," *Journal of Alloys and Compounds*, vol. 963, p. 171128, 2023.
[3] Q. Yin, Z. Liu, B. Wang, Q. Song, and Y. Cai, "Recent progress of machinability and surface integrity for mechanical machining Inconel 718: A review," *The International Journal of Advanced Manufacturing Technology*, vol. 109, pp. 215–245, 2020.
[4] C. Liu, M. Wan, W. Zhang, and Y. Yang, "Chip formation mechanism of Inconel 718: A review of models and approaches," *Chinese Journal of Mechanical Engineering*, vol. 34, pp. 1–16, 2021.

[5] K. Mahesh, J. T. Philip, S. N. Joshi, and B. Kuriachen, "Machinability of Inconel 718: A critical review on the impact of cutting temperatures," *Materials and Manufacturing Processes*, vol. 36, no. 7, pp. 753–791, 2021.
[6] C. Liu, M. Wan, and Y. Yang, "Simulation of the chip morphology together with its evolution in machining of Inconel 718 by considering widely spread cutting speed," *The International Journal of Advanced Manufacturing Technology*, vol. 116, pp. 175–195, 2021.
[7] C. Pérez-Salinas, L. N. L. de Lacalle, A. del Olmo, and C. S. Kumar, "The relationship between the cutting-edge, tool wear and chip formation during Inconel 718 dry cutting," *The International Journal of Advanced Manufacturing Technology*, vol. 132, no. 11, pp. 6001–6017, 2024.
[8] Z. Hao, B. Mu, and Y. Fan, "Cross-scale constitutive description and deformation mechanism in cutting nickel-based superalloy Inconel718," *International Journal of Material Forming*, vol. 18, no. 1, pp. 1–29, 2025.
[9] G. Arndt and R. H. Brown, "On the temperature distribution in orthogonal machining," *International Journal of Machine Tool Design and Research*, vol. 7, no. 1, pp. 39–53, 1967.
[10] A. F. Pedroso, N. P. Sebbe, R. D. Costa et al., "INCONEL® alloy machining and tool wear finite element analysis assessment: an extended review," *Journal of Manufacturing and Materials Processing*, vol. 8, no. 1, p. 37, 2024.
[11] M. Movahhedy, M. S. Gadala, and Y. Altintas, "Simulation of the orthogonal metal cutting process using an arbitrary Lagrangian–Eulerian finite-element method," *Journal of Materials Processing Technology*, vol. 103, no. 2, pp. 267–275, 2000.
[12] O. Pantalé, J. L. Bacaria, O. Dalverny, R. Rakotomalala, and S. Caperaa, "2D and 3D numerical models of metal cutting with damage effects," *Computer Methods in Applied Mechanics and Engineering*, vol. 193, no. 39-41, pp. 4383–4399, 2004.
[13] T. Ozel, I. Llanos, J. Soriano, and P. J. Arrazola, "3D finite element modelling of chip formation process for machining Inconel 718: comparison of FE software predictions," *Machining Science and Technology*, vol. 15, no. 1, pp. 21–46, 2011.
[14] X. Wang, C. Huang, B. Zou, H. Liu, H. Zhu, and J. Wang, "Dynamic behavior and a modified Johnson Cook constitutive model of Inconel 718 at high strain rate and elevated temperature," *Materials Science and Engineering: A*, vol. 580, pp. 385–390, 2013.
[15] F. Yi, R. Zhong, W. Zhu, R. Zhou, L. Guo, and Y. Wang, "Comparative study of friction in high-speed machining of titanium model alloys," *Lubricants*, vol. 13, no. 3, p. 113, 2025.
[16] W. B. Palmer and P. L. B. Oxley, "Mechanics of orthogonal machining," *Proceedings of the Institution of Mechanical Engineers*, vol. 173, no. 1, pp. 623–654, 1959.
[17] E. Muthu, K. Senthamarai, and S. Jayaba, Finite element simulation of machining a nickel-based superalloy: Inconel 718," *International Journal of Advanced Engineering Applications*, vol. 5, no. 3, pp. 22-27, 2012.
[18] V. Veeranaath, A. Anshuman, and S. Sethia, "Experimental Study and Finite Element Analysis of the Impact of Tool Edge Geometry in Orthogonal Machining of Super Alloy Inconel 718," in *IOP Conference Series: Materials Science and Engineering*, vol. 912, no. 3, p. 032032, IOP Publishing, 2020.
[19] G. C. Mouli, K. P. Marimuthu, and T. Jagadeesha, "2d finite element analysis of inconel 718 under turning processes," in *IOP Conference Series: Materials Science and Engineering*, vol. 912, no. 3, Art. no. 032021, IOP Publishing, 2020.
[20] U. M. R. Paturi, S. Methuku, S. S. Siripragada, Y. Sangishetty, and R. K. Gunda, "Finite element simulations of machinability parameters in turning of Inconel 718," *Materials Today: Proceedings*, vol. 38, pp. 2658–2663, 2021.
[21] Y. Liu, D. Xu, M. Agmell, R. M'Saoubi, A. Ahadi, J.-E. Stahl et al., "Numerical and experimental investigation of tool geometry effect on residual stresses in orthogonal machining of Inconel 718," *Simulation Modelling Practice and Theory*, vol. 106, p. 102187, 2021.
[22] B. Peng, T. Bergs, F. Klocke, and B. Döbbeler, "An advanced FE modeling approach to improve the prediction in machining difficult-to-cut material," *The International Journal of Advanced Manufacturing Technology*, vol. 103, pp. 2183–2196, 2019.
[23] A. F. V. Pedroso, V. F. C. Sousa, N. P. V. Sebbe, F. J. G. Silva, R. D. S. G. Campilho, R. C. M. Sales-Contini et al., "A brief review of INCONEL® alloys numerical analysis on predictability," *Procedia Computer Science*, vol. 232, pp. 1109–1120, 2024.
[24] T. Jadam, S. Datta, and M. Masanta, "Influence of cutting tool material on machinability of Inconel 718 superalloy," *Machining Science and Technology*, vol. 25, no. 3, pp. 349–397, 2021.
[25] Y. Zhang and J. Zheng, "Modelling and Finite Element Simulation of Ball-End Milling for Nickel-Based Superalloy Inconel 718," in *International Conference on Advances in Construction Machinery and Vehicle Engineering*, Singapore: Springer Nature Singapore, pp. 889–899, 2023.
[26] M. R. U. Rahim and P. K. Bharti, "Energy absorption characteristics of thin-walled sinusoidal corrugated tube using RSM-CCD," *Production Engineering Archives*, vol. 26, no. 4, pp. 144–153, 2020.
[27] M. R. U. Rahim and P. K. Bharti, "Buckling analysis of innovative corrugated column by using response surface methodology," *Acta Marisiensis. Seria Technologica*, vol. 18, no. 2, pp. 8-17, 2020.
[28] M. R. U. Rahim, M. F. Hasan, and M. N. Khan, "Optimization of square-based tapered twisted hollow tube using CCD approach in RSM," *Frontiers in Engineering and Built Environment*, vol. 5, no. 3, pp. 209–226, 2025.
[29] A. Thakur and S. Gangopadhyay, "State-of-the-art in surface integrity in machining of nickel-based super alloys," *International Journal of Machine Tools and Manufacture*, vol. 100, pp. 25–54, 2016.

[30] R. S. Pawade, S. S. Joshi, and P. K. Brahmankar, "Effect of machining parameters and cutting-edge geometry on surface integrity of high-speed turned Inconel 718," *International Journal of Machine Tools and Manufacture*, vol. 48, no. 1, pp. 15–28, 2008.
[31] P. J. Arrazola, T. Özel, D. Umbrello, M. Davies, and I. S. Jawahir, "Recent advances in modelling of metal machining processes," *CIRP Annals*, vol. 62, no. 2, pp. 695–718, 2013.
[32] E. O. Ezugwu and Z. M. Wang, "Titanium alloys and their machinability—a review," *Journal of Materials Processing Technology*, vol. 68, no. 3, pp. 262–274, 1997.
[33] T. Özel and D. Ulutan, "Prediction of machining induced residual stresses in turning of titanium and nickel-based alloys with experiments and finite element simulations," *CIRP Annals*, vol. 61, no. 1, pp. 547–550, 2012.
[34] D. A. Stephenson and J. S. Agapiou, *Metal cutting theory and practice*, CRC Press, 2018.
[35] F. Jafarian, D. Umbrello, and B. Jabbaripour, "Identification of new material model for machining simulation of Inconel 718 alloy and the effect of tool edge geometry on microstructure changes," *Simulation Modelling Practice and Theory*, vol. 66, pp. 273–284, 2016.
[36] P. J. Arrazola, "Investigations on the effects of friction modeling in finite element simulation of machining," *International Journal of Mechanical Sciences*, vol. 52, no. 1, pp. 31–42, 2010.
[37] S. Pervaiz, A. Rashid, I. Deiab, and M. Nicolescu, "Influence of tool materials on machinability of titanium-and nickel-based alloys: a review," *Materials and Manufacturing Processes*, vol. 29, no. 3, pp. 219–252, 2014.
[38] E. O. Ezugwu, "Key improvements in the machining of difficult-to-cut aerospace superalloys," *International Journal of Machine Tools and Manufacture*, vol. 45, no. 12-13, pp. 1353–1367, 2005.
[39] T. Kitagawa, A. Kubo, and K. Maekawa, "Temperature and wear of cutting tools in high-speed machining of Inconel 718 and Ti 6Al 6V 2Sn," *Wear*, vol. 202, no. 2, pp. 142–148, 1997.
[40] G. R. Johnson, "A constitutive model and data for metals subjected to large strains, high strain rates and high temperatures," in *Proceedings of the 7th International Symposium on Ballistics*, Netherlands, pp. 541–547, 1983.